Tuning the topological insulator states of artificial graphene

H. D. Scammell and O. P. Sushkov

School of Physics, University of New South Wales, Sydney, New South Wales 2052, Australia

We develop a robust, nonperturbative approach to study the band structure of artificial graphene. Artificial graphene, as considered here, is generated by imposing a superlattice structure on top of a two-dimensional hole gas in a semiconductor heterostructure, where the hole gas naturally possesses large spin-orbit coupling. Via tuning of the system parameters we demonstrate how best to exploit the spin-orbit coupling to generate time reversal symmetry protected topological insulator phases. Our major conclusion relates to a second set of topological Dirac bands in the band structure (with spin Chern number $C = 3$), which were not reliably obtainable in previous perturbative approaches to artificial graphene. Importantly, the second Dirac bands host more desirable features than the previously studied first set of Dirac bands (with $C = 1$). Moreover, we find that upon tuning of the system parameters, we can drive the system to the highly desirable regime of the topological flat band. We discuss the possibilities this opens up for exotic, strongly correlated phases.

I. INTRODUCTION

The quantum spin Hall effect, exhibited by time-reversal-symmetric topological insulators (TIs), is by now a well investigated topic. It has the desirable property of dissipationless spin currents along the edges of the sample, which is a fundamental ingredient for reversible quantum computation as well as for efficient spintronics applications. Realizations of two-dimensional (2D) TI states has been slow, with the best known examples arising in HgTe [1] and In As [2] quantum wells as predicted theoretically in Refs. [3–5]. As is well known, graphene was the first proposed material realization of a TI [6]; however within naturally occurring graphene the spin-orbit interaction is parametrically small. Therefore the topological gap, a measure of the stability of the TI state against (time-reversal-symmetric) disorder and thermal fluctuations, is small.

Aside from generating a robust TI state for the sake of technological advances, there has been a recent surge of interest in 2D topological band insulators for the purpose of realizing highly nontrivial strongly correlated phases of matter. In particular, the theoretical efforts have been focused on designing/predicting systems exhibiting (nearly) flat bands with nontrivial topology. Such conditions are expected to be sufficient to realize novel correlated phases: fractional Chern [7–12], fractional anomalous [8,13,14], and fractional topological insulators [15–19] (see reviews [20,21]), magnetic insulating phases [22–26] (review [24]), or superconducting/superfluid phases [27–31]. The logic is rather simple: the flat band implies that kinetic energy (which vanishes) is dominated by particle-particle interactions, even if they are "weak." Moreover, the flat bands support a macroscopic degeneracy—large density of states. Partial filling of such a flat band therefore becomes an exciting playground for strongly correlated physics. The prototypical example is the fractional quantum Hall effect, where the flat bands are the exactly flat Landau levels. Very recently, by analogy with

the fractional quantum Hall effect, there are mounting theoretical efforts to explain/predict fractional Chern insulators, the fractional anomalous Hall effect, and fractional TIs. To date, the pursuit for nearly flat bands with nontrivial topology has led to the proposal of several model Hamiltonians with at times peculiar properties such as complex or long-range hopping parameters, for which finding an experimental realization is a formidable task and requires fine tuning.

The present work considers a graphene simulator, *artificial graphene*, composed of a two-dimensional hole gas (2DHG) confined by a semiconductor quantum well, with an electrostatic potential of hexagonal symmetry etched onto a metallic top gate. This *superlattice* structure generates a graphene-like electronic band structure. There have been numerous graphene simulator proposals: cold atoms [32–35], lithographic [36–41], and more [42–48]; for a review see [49]. Our primary motivation is to optimize (with respect to system parameters) the robustness of the topological insulator phase, i.e., the topological gap. To this end, a hole gas, as opposed to an electron gas, is the obvious choice since the holes in semiconductor heterostructure systems possess effective spin-3/2 angular momentum, and thus naturally experience larger spin-orbit coupling than the corresponding spin-1/2 electrons. Our secondary motivation is to search for nearly flat bands with nontrivial topology. Due to the nature of the dispersion of the 2DHG we will see that generating a nearly flat band once the superlattice is imposed becomes a natural feature of the artificial graphene spectrum—and does not require fine tuning.

Artificial graphene (as defined here) is a readily tunable system and hence has already been proposed as a candidate material to exhibit a TI state [50] and a Chern insulator under (in-plane) applied field [51], as well as realizing a topological semimetal [52]. We are concerned with the TI state suggested in [50], whereby such calculations have been based on a perturbative theory of the 2DHG—valid in the
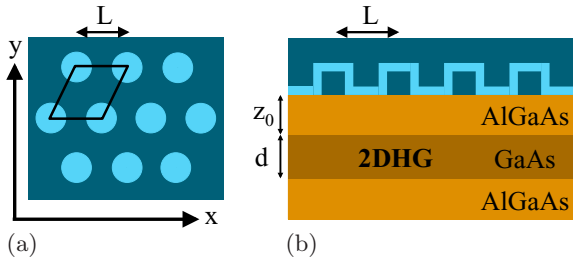
FIG. 1. Schematic view of artificial graphene. (a) A top view of the superlattice etched into the the metallic top gate. Blue dots represent positive potentials (antidots). L is the lattice spacing. (b) A cross section of the AlGaAs-GaAs-AlGaAs heterostructure. d is the quantum well confined length; z_0 is the separation length between the superlattice top gate and the 2DHG.

limit of small spin-orbit interaction—which then enters into the band structure calculations of the superlattice, artificial graphene. Although these perturbative approaches no doubt capture the essential qualitative physics, in the limit of large spin-orbit coupling, which is the most desirable for technological application or to pursue the topological flat band regime, they become unreliable. To address this gap in the literature, the present work develops a nonperturbative description of artificial graphene, valid at arbitrarily large spin-orbit coupling. Hence, as experimental efforts move closer to explicit realization, the necessity of the present work is self-evident.

To conclude this introductory passage, it is important to make explicit the differences and expected overlap of the present results with those obtained for the electron-doped, i.e., 2DEG, artificial graphene considered in Ref. [53]. The most important difference between the 2DHG and 2DEG, having in mind a heterostructure such as AlGaAs-GaAs-AlGaAs, is that the electrons of the 2DEG have negligible spin-orbit interaction, whereas the holes of the 2DHG host a substantial spin-orbit interaction. On the other hand, one expects electrostatic screening properties within a 2DEG and 2DHG to be essentially equivalent. Reference [53] has demonstrated that screening has a negligible effect on the band structure of 2DEG artificial graphene. Armed with this knowledge, the present paper ignores screening effects for the 2DHG analog.

The next section, Sec. II, provides a self-contained introduction to the technical aspects of the paper, in which we outline the construction of artificial graphene, the necessary technical details of the 2DHG, and the previous perturbative approach [50], and finally we develop our new nonperturbative approach to artificial graphene. Having established these necessary preliminaries we move on to our results in Secs. III and III C.

II. MATHEMATICAL PRELIMINARIES

A. Key parameters of artificial graphene

To adequately set the stage for the mathematical details to follow, we briefly outline the schematics of artificial graphene, and in doing so establish the key parameters available for tuning; see Fig. 1. First, we consider a 2DHG having in mind, e.g., an AlGaAs-GaAs-AlGaAs quantum well. The confinement is along the z axis, leaving the x-y plane for free motion;

this is the 2DHG. For the bulk of the results/calculations we take the confinement to be a rectangular quantum well of width d. We will also perform semianalytics for the case of a triangular well. Next, a periodic electrostatic potential of triangular symmetry is etched onto a metal plate on top of the 2DHG; this is the superlattice. The lattice parameter (henceforth the *superlattice parameter*) is L. The separation along the z axis of the superlattice top gate from the 2DHG is z_0. Although z_0 plays a role [53], we will fix its value and not consider it further. Finally, we denote the magnitude of the electrostatic potential by W. Ultimately, it is the ratio of d/L that controls the spin-orbit interaction, and we can choose W freely; this provides us with two tuning handles: d/L and W. Also note that tuning z_0 is equivalent to tuning W.

B. 2DHG

We consider a 2DHG confined along the z axis by the quantum well potential:

$$V(z) = \begin{cases} 0, & z \in (-d/2, d/2), \\ \infty, & \text{otherwise.} \end{cases} \tag{1}$$

For this confinement we set the characteristic momentum and energy scale to be

$$k_0 = \frac{2}{d}, \quad E_0 = \frac{\gamma_1 k_0^2}{2m} \equiv \frac{k_0^2}{2m^*}, \tag{2}$$

where m is the electron mass in vacuum, γ_1 is one of the Luttinger parameters entering the Hamiltonian below, and we have introduced the effective mass m^* to facilitate later discussion. The energy scale for a quantum well of width $d = 20$ nm is $E_0 = 2.6$ meV. It is important to note that this energy scales as $E_0 \sim 1/d^2$.

The holes posses an ultrarelativistic spin-orbit coupling, and can be described by the Luttinger Hamiltonian in the axial approximation, i.e., $U(1)$ symmetry in-plane. The axial approximation is useful for quasi-2D systems with frozen dynamics along one direction, in the present case, the z axis. The Luttinger Hamiltonian we consider is [54]

$$H_{\text{2DHG}} = H_0 + H_{\text{SO}},$$
$$H_0 = \left[\gamma_1 + 2\gamma_2\left(\frac{5}{2} - S_z\right)\right]\frac{k_z^2}{2m}$$
$$\quad + \left[\gamma_1 - \gamma_2\left(\frac{5}{4} - S_z\right)\right]\frac{\boldsymbol{k}^2}{2m} + V(z),$$
$$H_{\text{SO}} = -\frac{\gamma_2 + \gamma_3}{8m}\left(k_+^2 S_-^2 + k_-^2 S_+^2\right)$$
$$\quad - \frac{\gamma_3}{4m}\{k_z, \{S_z, k_+ S_- + k_- S_+\}\}, \tag{3}$$

where S_x, S_y, S_z are angular momentum 3/2 operators, $S_\pm = S_x \pm iS_y$, we use bold font to express the in-plane momenta $\boldsymbol{k} = (k_x, k_y)$, and $k_\pm = k_x \pm ik_y$. In the expression for H_{2DHG} (3), we have chosen to separate the components H_0 and H_{SO} (which accounts for spin-orbit interactions). This is merely to help illustrate the following technical step: we perform exact diagonalization of H_{2DHG} in the basis of wave functions obtained from H_0. A later step will be to project the wave functions of H_{2DHG} onto the superlattice potential; the details will be provided in Sec. II C.
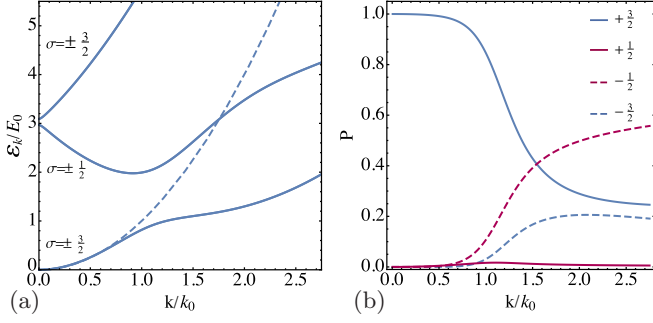
FIG. 2. (a) The dispersion of holes in the semiconductor quantum well: Solid lines are the dispersions obtained from the multiband Luttinger Hamiltonian approach (3). The dashed line corresponds to the single-band, quadratic approximation, i.e., using $\mathcal{E}_k = k^2/(2m^*)$. The projections of the total angular momentum are denoted σ, which at $k = 0$ are identically the physical spin projections. (b) A plot of the relative weight of the projection onto each physical spin component S_z, and their dependence on $\mathbf{k}$, in the lowest-band Kramers spin state $|l = 0, \sigma_l = +3/2, \mathbf{k}\rangle \equiv |\uparrow, \mathbf{k}\rangle$.

Some effort has been made [54] to obtain semianalytic expressions for the H_{2DHG} wave functions, which saves computational time and provides a clearer mathematical picture. We outline the results obtained previously [54]: the wave functions are labeled by a $\mathbf{k}$ (a good quantum number) as well as the energy-level index l and corresponding spin index σ_l, which corresponds to the physical spin projection only at $\mathbf{k} = 0$. The wave functions of H_{2DHG} for quantum well confinement in the z direction read

$$|l, \sigma_l, \mathbf{k}\rangle = e^{i k r} \sum_{S_z} \hat{k}_+^{(\sigma_l - S_z)} \sum_n a_{l,n,S_z}(k) |S_z, n\rangle, \quad (4)$$

where, importantly, the argument of $a_{l,n}$ is $k \equiv |\mathbf{k}|$, and all phase dependence on the 2D momentum plane is stored in the prefactor $\hat{k}_+^{(\sigma_l - S_z)}$ such that $\hat{k}_\pm \equiv (k_x \pm i k_y)/|\mathbf{k}|$, which greatly simplifies the band structure computations. The ket, $|S_z, n\rangle$, accounts for the basis of the four $S_z = \pm 3/2, \pm 1/2$ spinors and the infinite set of harmonics, enumerated by the non-negative integers n, due to confinement along the z axis.

To be explicit, Fig. 2(a) shows the first three dispersion levels $l = 0, 1, 2$ and the corresponding spin indices $\sigma_l = \pm 3/2, \pm 1/2, \pm 3/2$ (for the quantum well potential). If one considers just the $l = 0$ subspace, then it is enlightening to regard this as a pseudospin-1/2, such that $|l = 0, +3/2, \mathbf{k}\rangle = |\uparrow, \mathbf{k}\rangle$ and $|l = 0, -3/2, \mathbf{k}\rangle = |\downarrow, \mathbf{k}\rangle$. Due to time-reversal symmetry (denoted $\mathcal{T}$), $\mathcal{E}_{\uparrow, \mathbf{k}} = \mathcal{E}_{\downarrow, -\mathbf{k}}$; i.e., $|\uparrow, \mathbf{k}\rangle$ and $|\downarrow, \mathbf{k}\rangle$ are Kramers partners. (Note: Throughout the text we call the two possible angular momentum eigenstates/projections of any given dispersion band l the *Kramers spin*.) Moreover, for the quantum well confinement there is an inversion symmetry or parity ($\mathcal{P}$), such that $\mathcal{E}_{\uparrow, \mathbf{k}} = \mathcal{E}_{\uparrow, -\mathbf{k}}$.

Figure 2(b) shows the probabilities of each physical spin (S_z) component of the particular state $|l = 0, +3/2, \mathbf{k}\rangle = |\uparrow, \mathbf{k}\rangle$. The probabilities of each S_z are expressed as [using notation introduced in Eq. (4)]

$$P_{l, \sigma_l, S_z} = \sum_n |a_{l,n,S_z}(k)|^2, \quad (5)$$

which are normalized for each index $\{l, \sigma_l\}$ such that $\sum_{S_z} P_{l, \sigma_l, S_z} = 1$. We see from Fig. 2(b) that all spin components are mixed via $\hat{J} = 1, 2, 3$ (dipole, quadrupole, octupole).

It is also instructive to contrast the exact diagonalization results of Eq. (4) [and also partially represented in Fig. 2(b)] to results of perturbation theory [50]. From perturbation theory, the wave functions of the $l = 0$ Kramers doublet are given as

$$|\uparrow, \mathbf{k}\rangle = \left[\left|+\frac{3}{2}\right\rangle + \beta k_+^2 \left|-\frac{1}{2}\right\rangle\right] e^{i\mathbf{k} \cdot \mathbf{r}},$$

$$|\downarrow, \mathbf{k}\rangle = \left[\left|-\frac{3}{2}\right\rangle + \beta k_-^2 \left|+\frac{1}{2}\right\rangle\right] e^{i\mathbf{k} \cdot \mathbf{r}}, \quad (6)$$

$$\beta = \frac{\sqrt{3} d^2}{4\pi}.$$

Hence, in this approach we clearly see that only mixing via $\hat{J} = 2$ (quadrupole) selection occurs, i.e., $S_z = \pm 3/2$ and $\mp 1/2$. Moreover, the wave functions (6) are valid only if $\beta^2 k^4 \ll 1$.

We will also consider a triangular well confinement by introducing the confinement potential

$$V(z) = \begin{cases} e\mathcal{E}z, & z > 0, \\ \infty, & \text{otherwise.} \end{cases} \quad (7)$$

For this confinement we set the characteristic momentum and energy scale to be

$$k_0 = \frac{1}{2} m e \mathcal{E}, \quad E_0 = \frac{\gamma_1 k_0^2}{2m}. \quad (8)$$

This potential explicitly breaks $\mathcal{P}$ and with it, $\mathcal{E}_{\uparrow, \mathbf{k}}^{\text{tri}} \neq \mathcal{E}_{\uparrow, -\mathbf{k}}^{\text{tri}}$, which removes the double degeneracy of the energy at a given momentum. We perform exact diagonalization of the Luttinger Hamiltonian Eq. (3) subject to the triangular confinement; the energy spectrum is shown in Fig. 3(a). In Fig. 3(b) we show the energy splitting between the two $l = 0$ bands; we call it the *Rashba splitting* and denote it by Δ_R. The important point here is that $\mathcal{P}$-breaking confinement Eq. (7) generates the Rashba spin-orbit interaction. In Sec. III C we will take a semianalytic approach and consider just these two lowest bands in an effective Hamiltonian.
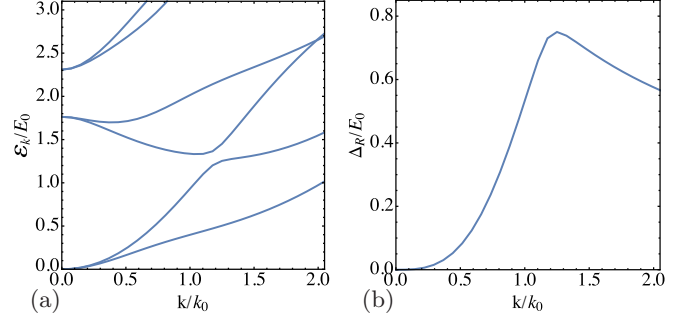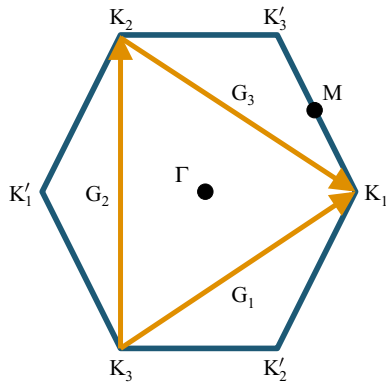

FIG. 3. (a) Spectrum of 2DHG in the triangular well confinement of Eq. (7). (b) Rashba splitting: The energy splitting between the two lowest ($l = 0$) dispersion bands in (a).

FIG. 4. Brillouin zone. $\boldsymbol{G}_i$ are vectors connecting zone corners $\boldsymbol{K}_j$. $\boldsymbol{K}'_j$ are parity reflections of $\boldsymbol{K}_j$.

C. Superlattice theory

We describe the superlattice potential via a harmonic approximation (for more details see Ref. [53]),

$$\mathcal{U}(\boldsymbol{r}) = 2W \sum_{t=1}^{3} \cos(\boldsymbol{G}_t \cdot \boldsymbol{r}), \tag{9}$$

where W is a constant that determines the strength of the potential. The vectors $\boldsymbol{G}_i$ [$|\boldsymbol{G}_i| = 4\pi/(\sqrt{3}L)$] are the reciprocal lattice vectors connecting corners of the hexagonal Brillouin zone $\boldsymbol{K}_j$ [$|\boldsymbol{K}_j| = 4\pi/(3L)$], as shown in Fig. 4. It is convenient to introduce the energy scale of the superlattice,

$$E_L = \frac{\boldsymbol{K}_j^2}{2m^*} = \frac{8\pi^2}{9L^2 m^*}. \tag{10}$$

We describe the problem by the *superlattice Hamiltonian* operator,

$$\hat{\mathcal{H}} = \hat{\mathcal{E}}_{2\mathrm{DHG}} + \hat{\mathcal{U}}(\boldsymbol{r}), \tag{11}$$

whereby $\hat{\mathcal{E}}_{2\mathrm{DHG}}$ represents the *kinetic energy* operator, which encodes the dispersions of holes in the 2DHG; i.e., its matrix elements (in a given basis) are the eigenvalues of $H_{2\mathrm{DHG}}$ (3), also shown in Fig. 2(a). The potential $\hat{\mathcal{U}}$ is given by Eq. (9), except we use a hat/operator notation to imply that we need to project these operators onto a particular basis. We take the wave functions of $H_{2\mathrm{DHG}}$ (3) as this basis, and project the superlattice Hamiltonian $\hat{\mathcal{H}}$ onto them. Previously in Eq. (4) we used the notation $|l, \sigma_l, \boldsymbol{k}\rangle$ for the $H_{2\mathrm{DHG}}$ wave functions; now due to the superlattice potential $\hat{\mathcal{U}}(\boldsymbol{r})$ we must attach an extra index i (such that $|l, \sigma_l, \boldsymbol{k}\rangle \rightarrow |l, \sigma_l, \boldsymbol{k}, i\rangle$) that labels sites in the momentum grid $\boldsymbol{k}_i = \boldsymbol{k} + \boldsymbol{g}_i$, where the discrete momentum space grid $\boldsymbol{g}_i \in \{n_1 \boldsymbol{G}_1 + n_2 \boldsymbol{G}_2 + n_3 \boldsymbol{G}_3 : n_i \in \mathbb{Z}\}$ is the space of degenerate momentum points. Note: $\langle l, \sigma_l, \boldsymbol{k}, i| \hat{\mathcal{E}}_{2\mathrm{DHG}} |m, \sigma_m, \boldsymbol{k}, j\rangle$ is diagonal in all indices and $\langle l, \sigma_l, \boldsymbol{k}, i| \hat{\mathcal{U}}(\boldsymbol{r}) |m, \sigma_m, \boldsymbol{k}, j\rangle$ is traceless (since it is traceless in the indices i, j).

1. Perturbative, single-band theory

For completeness, we present here the effective Hamiltonian derived in [50], which will allow us to most easily con-

trast our nonperturbative Hamiltonian presented in Eq. (14). Applying the procedure outlined above to the simplest case: Considering just three degenerate points (of the same parity) $\boldsymbol{K}_1, \boldsymbol{K}_2, \boldsymbol{K}_3$, we project the superlattice Hamiltonian (11) onto the perturbative wave functions of Eq. (6), which have just $l = 0$, $\sigma_{l=0} = \pm 3/2$ components, and find

$$\mathcal{H}_{i,j,l,m} = \langle \sigma_l, \boldsymbol{k}, i| \hat{\mathcal{H}} |\sigma_m, \boldsymbol{k}, j\rangle,$$

$$(\mathcal{H}_{i,j,l,m}) = \begin{pmatrix} \mathcal{E}(\boldsymbol{k} + \boldsymbol{K}_1) & W & W \\ W & \mathcal{E}(\boldsymbol{k} + \boldsymbol{K}_2) & W \\ W & W & \mathcal{E}(\boldsymbol{k} + \boldsymbol{K}_3) \end{pmatrix} \otimes \mathbb{I}$$

$$+ \frac{1}{\sqrt{3}} \eta \begin{pmatrix} 0 & i & -i \\ -i & 0 & i \\ i & -i & 0 \end{pmatrix} \otimes \tau_z, \tag{12}$$

where $\mathbb{I}$ is the two-dimensional identity matrix and τ_z is the usual Pauli matrix, both of which act on the physical spin/Kramers doublet subspace. In this approximation, the diagonal elements are just quadratic dispersions $\mathcal{E}(\boldsymbol{k}) = \boldsymbol{k}^2/(2m^*)$; we refer to this as the *single-band, quadratic approximation*. The coefficient $\eta = 3/2\beta^2 K_1^4 W$, with β taken from Eq. (6) and W from Eq. (9), determines the strength of the spin-orbit coupling. Consider $\boldsymbol{k} = 0$, whereby the diagonal elements are equal since $|\boldsymbol{K}_j| = 4\pi/(3L)$; upon setting $\eta = 0$ we find that there is a doubly degenerate eigenvalue $\{-W, -W, 2W\}$ of $\mathcal{H}$ in (12): this is the Dirac point [37,50]. Projecting the Hamiltonian (12) onto the doubly degenerate subspace, allowing for $\eta \neq 0$, and performing a small $\boldsymbol{k}$ expansion about $\boldsymbol{K}_1, \boldsymbol{K}_2, \boldsymbol{K}_3$ gives the Kane-Mele-like Hamiltonian [50],

$$H_D = -v(p_x \sigma_y + p_y \sigma_z) \otimes \mathbb{I} - \eta \sigma_x \otimes \tau_z, \tag{13}$$

where σ_i are Pauli matrices acting on the pseudospin space generated by the doubly degenerate eigenvalues $\{-W, -W\}$ of $\mathcal{H}$ in (12). From the Dirac-like Hamiltonian (13) one finds [50] that the spin-orbit gap is given by $\Delta_{SO} = 2\eta \sim (d/L)^4 W$. In Sec. III B, we will compare this perturbative result for Δ_{SO} to our nonperturbative results obtained from the Hamiltonian (14), presented next.

2. Nonperturbative, multiband theory

The so-called *multiband approximation* is our primary technical development, and can be conveniently understood as the nonperturbative extension of the Hamiltonian (12) derived above. In the multiband approximation, we use the exact diagonalization results for the Luttinger Hamiltonian (3) wave functions, which are compactly expressed in Eq. (4), and project the superlattice Hamiltonian operator (11) onto this basis. Such a procedure generates the following matrix structure,
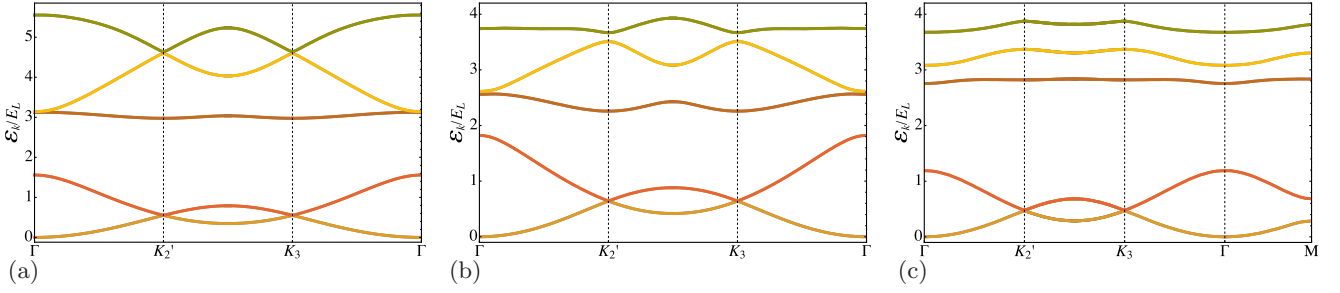
FIG. 5. Evolution of the miniband spectrum upon tuning d/L and W. All bands are doubly degenerate due to $\mathcal{T}$ and $\mathcal{P}$ symmetry; each band possesses a pair of Kramers spins, which we can refer to as spin $\uparrow$ and $\downarrow$. (a) Corresponds to the *Dirac regime*, with small spin-orbit interaction set by the small ratio $d/L = 1/8$. We call the lower (upper) two minibands in the vicinity of the Brillouin zone corners $\boldsymbol{K}, \boldsymbol{K}'$, the first (second) Dirac points. The superlattice potential (9) has strength $W = 2E_L$, with E_L from (10), chosen to produce steep second Dirac cones. (b) The parameters, $d/L = 1.75/8$ and $W = E_L$, are chosen to produce a prominent TI gap at the second Dirac cones. (c) Demonstration of a nearly flat, topologically nontrivial band; the second highest in energy miniband is seen to become nearly flat upon choosing parameters $d/L = 1.75/8$ and $W = 3E_L$, while the Chern numbers for each of the Kramers spins in this band are $C_{\uparrow,\downarrow} = \pm 3$. Note: The topological band gaps at the first Dirac points are nonzero, yet smaller than the thickness of the lines; see Fig. 6(a).

$$\mathcal{H}(\boldsymbol{k})_{(i,j),(l,m),(\sigma_l,\sigma_m)} = \langle \boldsymbol{k}, j, l, \sigma_l | \hat{\mathcal{H}} | \boldsymbol{k}, i, m, \sigma_m \rangle = \langle \boldsymbol{k}, j, l, \sigma_l | \hat{\mathcal{E}} | \boldsymbol{k}, i, m, \sigma_m \rangle + \langle \boldsymbol{k}, j, l, \sigma_l | \hat{\mathcal{U}}(\boldsymbol{r}) | \boldsymbol{k}, i, m, \sigma_m \rangle$$

$$= \mathcal{E}_{i,l,\sigma_l}(\boldsymbol{k}_i) \delta_{i,j} \otimes \delta_{l,m} \otimes \delta_{\sigma_l,\sigma_m} + \mathcal{U}_{(i,j),(l,m),(\sigma_l,\sigma_m)}(\boldsymbol{k}_i) \delta_{\sigma_l,\sigma_m},$$

$$\mathcal{U}(\boldsymbol{k})_{(i,j),(l,m),(\sigma_l,\sigma_m)} = W \sum_{t=1}^{3} \delta(\boldsymbol{k}_i - \boldsymbol{k}_j \pm \boldsymbol{G}_t) \sum_{S_z,S_z'} \sum_{n,n'} \hat{k}_{j,-}^{(\sigma_l - S_z')} \hat{k}_{i,+}^{(\sigma_m - S_z)} a_{l,n',S_z'}^{*}(|\boldsymbol{k}_j|) a_{m,n,S_z}(|\boldsymbol{k}_i|) \, \langle S_z', n' | S_z, n \rangle \qquad (14)$$

$$= W \sum_{t=1}^{3} \delta(\boldsymbol{k}_i - \boldsymbol{k}_j \pm \boldsymbol{G}_t) \sum_{S_z} \sum_{n} \hat{k}_{j,-}^{(\sigma_l - S_z)} \hat{k}_{i,+}^{(\sigma_m - S_z)} a_{m,n,S_z}^{*}(|\boldsymbol{k}_j|) a_{l,n,S_z}(|\boldsymbol{k}_i|),$$

where a given matrix element of the kinetic matrix $\mathcal{E}_{i,l,\sigma_l}(\boldsymbol{k}_i)$ is evaluated directly from the underlying 2DHG spectrum, also shown in Fig. 2(a). We note that previous approaches [50] have taken a quadratic approximation, such that $\mathcal{E}_{i,l,\sigma_l}(\boldsymbol{k}_i) = k_i^2/(2m^*)$, which we sketch via the dashed line in Fig. 2(a). To generate a large topological gap, we are required to consider momentum and energy scales that are beyond the validity of the single-band, quadratic approximation. Moreover, the wave functions obtained in perturbation theory only account for quadrupole mixing, which is only valid for small $k/k_0 < 1$, as seen in Fig. 2(b). This motivates our present construction over previous approaches [50].

That completes the mathematical preliminaries. The remaining discussion and results are centered around the so called first and second sets of Dirac bands, which correspond to the lower and upper two bands, respectively, shown in Fig. 5. The opening of a topological band gap within, and the subsequent evolution of the second Dirac bands, is our main finding. We dedicate Sec. III A to this point. However, since the first Dirac bands have been considered previously using perturbation theory [50], we will discuss two aspects of the first Dirac bands: Sec. III B provides a comparison between our results and the perturbative results, while Sec. III C considers the influence of $\mathcal{P}$ breaking. Finally, Sec. IV contains our conclusions and further discussion. Wherever possible, we present results in physical scales coincident with those currently experimentally achievable.

III. RESULTS

Our results are obtained by varying the two available tuning handles (recall from Sec. II A): the ratio d/L and the strength W of the superlattice potential (9). We will now discuss the influence of each. For convenience, in the vicinity of the Brillouin zone corners $\boldsymbol{K}, \boldsymbol{K}'$, we call the (nearly) band touching points of the first (second) Dirac bands the *first (second) Dirac points*—or just 1DP (2DP).

Tuning the ratio d/L determines the energy/momentum scale at which the Dirac points occur relative to the underlying 2DHG spectrum, i.e., which part of the 2DHG spectrum is band folded at the Dirac point. As the ratio d/L is increases from zero, the anticrossing *kink* in the 2DHG spectrum, Fig. 2(a), moves from higher energies down towards the Dirac points of the corresponding band structure, i.e., after imposition of the superlattice. At the same time, one can see that the wave functions are becoming maximally mixed at the scale $k \sim k_0$, Fig. 2(b); i.e., the pure spin projections $\pm 3/2, \pm 1/2$ are heavily mixed for $k \sim k_0$, due to spin-orbit coupling. Hence the location of the kink relative to the Dirac point provides a qualitative indication of the effective strength of the spin-orbit coupling at the Dirac point; the closer the kink the larger the spin-orbit coupling.

The second tuning handle we have at our disposal is the parameter W. Tuning the energy scale of the potential W relative to the characteristic energy of the Brillouin zone E_L (10) provides a means to control the *steepness* of the Dirac

cones, i.e., the effective velocity in the vicinity of the Dirac points. For example, in Fig. 5(a) we choose $W = 2E_L$ to approximately optimize the steepness of the 2DP; this choice was also made in [53]. Moreover, by taking $d/L = 1/8$ we are sitting in the quadratic band regime, and in this limit we verify that our results reproduce Ref. [53].

With the freedom of two tuning handles, d/L and W, there are many quantitatively distinct band structures we can present. For conceptual clarity as well as for ease of presentation we discuss what we consider to be the two most important qualitatively distinct regimes: (i) The anticrossing is band folded to be in the vicinity of the first Dirac points (1DP), such that $k_0 = 2/d \approx K_{1DP} = 4\pi/(3L)$, and hence $d/L \approx 1/2$. (ii) The anticrossing is coincident with the second Dirac points (2DP), such that $k_0 \approx K_{2DP} = 2K_{1DP}$, and hence $d/L \approx 1/4$.

A. $\mathcal{P}$ and $\mathcal{T}$ symmetric: Second Dirac bands

The current experimental limitations are approximately $10 \lesssim d \lesssim 30$ nm and $L \gtrsim 40$ nm. Moreover, the energy scale of the problem is set by $E_0 \sim 1/d^2$ (or equivalently $E_L \sim 1/L^2$ for fixed d/L), inspiring us to consider the lower limit of the well confinement $d \sim 10$ nm to maximize the topological band gaps.

Let us consider $L/d \sim 4$, which is both (i) achievable experimentally and (ii) places the anticrossing at the 2DP. Figure 5 shows the evolution of the band structure with parameters $d/L = 1/8, 1.75/8, 1.75/8$ and $W = 2E_L, E_L, 3E_L$ for Figs. 5(a), 5(b) and 5(c), respectively. Figure 5(a) corresponds to the Dirac regime with vanishing spin-orbit gap; this result approximately coincides with the results obtained previously [53] assuming no spin-orbit interaction. Figure 5(b) shows the opening of a significant topological gap at the 2DP, while the topological gap remains vanishingly small at 1DP (although it is still nonzero). This result has not been discussed previously, and represents one of our primary conclusions. From here we conclude that tuning the Fermi energy to lie within the spin-orbit band gap of the second set of Dirac bands represents a more suitable topological insulator than tuning to the first set of Dirac bands. *Suitability* here refers to the size of the topological gap and hence the state's resilience to thermal fluctuations and disorder. We find that the spin-orbit band gap Δ_{SO} (evaluated at the $\mathbf{K}$ points) of the 2DP is largest in Fig. 5(c), which corresponds to parameters $\{d/L, W\} = \{1.75/8, 3E_L\}$. The gap is seen to be $\Delta_{SO} \approx 0.5E_L$, which corresponds to $\Delta_{SO} \approx 1.1$ meV at $d = 10$ nm and $L = 46$ nm. Again, for fixed ratio d/L the energy scale of the system $E_L \propto 1/L^2$, and hence motivation for small quantum well confinement length d and superlattice spacing L, is apparent.

Tuning the Fermi energy to lie in the gap of the 1DP or 2DP, we can approximate the corresponding hole density as $\langle n \rangle = 4/(\sqrt{3}L^2)$ or $16/(\sqrt{3}L^2)$, respectively. Experimentally achievable hole densities are currently $n \approx 10^{11}$ cm^{-2} [55]. Table I presents the hole carrier densities corresponding to tuning the Fermi energy (E_F) to the first and second Dirac points of Fig. 5, from which we see that the 2DP supports realistic hole densities, and in this sense is more suitable than the 1DP.

Each Kramers spin in the lower band of the second Dirac bands has Chern number [56] $C_{\uparrow,\downarrow} = \pm 3$, implying there are

TABLE I. Hole carrier densities $\langle n \rangle$ for E_F tuned to the 1DP and 2DP of Figs. 5(a), 5(b) and 5(c), calculated for quantum well confinement $d = 10$ nm and 20 nm.

d	E_F	Fig. 5(a)	Figs. 5(b) and 5(c)
10 nm	1DP	3.6×10^{10} cm^{-2}	1.1×10^{11} cm^{-2}
	2DP	1.4×10^{11} cm^{-2}	4.4×10^{11} cm^{-2}
20 nm	1DP	9.0×10^{9} cm^{-2}	2.7×10^{10} cm^{-2}
	2DP	3.6×10^{10} cm^{-2}	1.1×10^{11} cm^{-2}

three pairs of topologically protected edge modes (when the Fermi energy is tuned to lie in the spin-orbit band gap of the second Dirac bands). Moreover, in Fig. 5(c) we see that the topologically nontrivial bands of the second Dirac bands are nearly flat. The nearly flat band generates a high density of states, and since the kinetic energy scale (bandwidth) is vanishing the particle-particle interactions become important. On general grounds there is expected to be an instability towards an ordered strongly correlated phase with leading candidates suggested in the literature; fractional TI [15–19], ferromagnetism [22,23,25,26], or charge density wave [11,24,57]. Explicit calculation of particle-particle interactions or strong correlation effects is beyond the scope of the present work, which is manifestly a single-particle theory. Instead such a calculation would be more suited to an effective quantum field theoretic approach, although this typically comes at the cost of losing microscopic details. Alternatively, to find which instability dominates we hope that the present work will motivate experimental searches for strongly correlated phases in artificial graphene. Finally, we mention that in the limit of flat bands, one cannot rely on single-particle theory and our above discussion may seem hopeless. However, note that single-particle physics predicts flat Landau levels, which are then the basis for the understanding of the strongly correlated fractional quantum Hall phase. This analogy has inspired our above claims as well as the many other studies of fractional TIs [15–19].

B. $\mathcal{P}$ and $\mathcal{T}$ symmetric: First Dirac bands

We now consider the first Dirac bands. The purpose of this subsection is to compare our results to those obtained previously in Ref. [50]. For the 1DP, we find the Chern numbers to be $C_{\uparrow,\downarrow} = \mp 1$, which is consistent with the edge modes calculated analytically in [50]; there they find a single pair of counterpropagating, opposite (Kramers) spin edge modes. For clarity, we depict such edge modes schematically by the black dashed lines in Fig. 6.

We provide Figs. 6(a) and 6(b), with ratios $d/L = 1/4$ and $d = 1/2$, to demonstrate the sensitive dependence of the topological gap on this ratio. As explained, the dramatic enhancement of the gap occurs when the kink corresponds to the 1DP. Focusing on Fig. 6(b), the spin-orbit gap is seen to be $\Delta_{SO} \approx 0.3E_L$, which converts to $\Delta_{SO} \approx 0.8$ meV for the feasible system parameters: $d = 20$ nm and $L = 40$ nm. This result compares well with $\Delta_{SO} \approx 0.2E_L$ obtained in Ref. [50], even though $d/L = 2$ corresponds to the upper limit of the validity of the perturbative results.
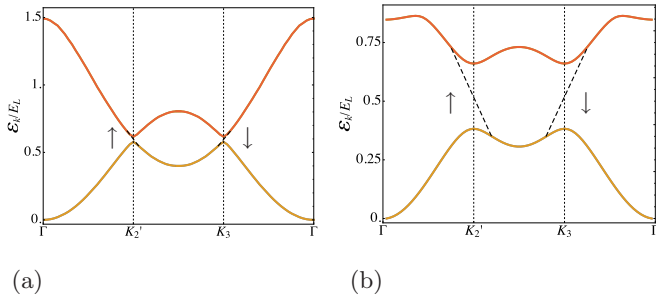
FIG. 6. Comparison of the first Dirac points with parameters (a) $d/L = 1/4$, (b) $d/L = 1/2$, with the strength of the potential the same for both cases, $W = 2E_{L=4}$. The black dotted lines connecting the upper and lower bands in each figure are a schematic representation of the edge modes. The arrows indicate the Kramers spin of the edge modes.
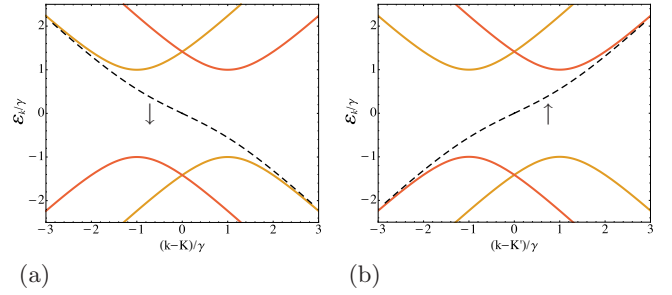

FIG. 7. Effect of Rashba ($\mathcal{P}$ breaking) on the band structure. The bulk (solid lines) and edge (dashed lines) bands are evaluated in the vicinity of (a) the $\mathbf{K}$ points, and (b) the $\mathbf{K'}$ points. We take the parameters $\eta = \gamma = v = 1$ in Eq. (16). The arrows indicate the Kramers spin of the edge modes.

C. $\mathcal{P}$ broken: First Dirac bands

We now turn to the influence of explicit parity breaking. We consider specifically the triangular well confinement of Eq. (7), whereby $\mathcal{T}$ symmetry remains intact while $\mathcal{P}$ is explicitly broken. The results of this section are limited to the perturbative approximation, via an extension of Eq. (12), and hence only provide information for the 1DP. Motivation for this calculation is to obtain a qualitative understanding of the effect of parity breaking on the edge modes, since almost all experimentally produced confining potentials possess some degree of inhomogeneity and with it $\mathcal{P}$ breaking (as well as that triangular wells are purposefully designed).

We use a semianalytic approach to elucidate the key influence of $\mathcal{P}$ breaking and Rashba spin-orbit coupling (see Fig. 7). As outlined in Ref. [50] and Sec. II C 1, we construct a low-energy effective Hamiltonian in the vicinity of the $\mathbf{K}_j$ points ($\mathbf{K'}_j$ is easily obtained thereafter), which is valid only for small $\mathbf{k}$ about this point; the result is shown in Eq. (13). See also the original work [50]. Next, the $\mathcal{P}$-breaking (cubic) Rashba interaction is introduced via

$$\delta H_R = -\frac{i}{2}\alpha\left(k_+^3\tau_- - k_-^3\tau_+\right), \quad (15)$$

where the raising operators $\tau_\pm = \tau_x \pm i\tau_y$ act on the two spins in the lowest $l = 0$ subspace of the underlying 2DHG dispersion [i.e., the lowest dispersion branch of Fig. 2(a)], and α is an effective interaction constant. Evaluating the projection of δH_R onto a plane wave basis, and following up with a projection into the pseudospin space (exactly following the steps described after Eq. (13) and given in more detail in [50]), we obtain the effective Hamiltonian,

$$H_R = -v(k_x\sigma_z + k_y\sigma_x) \otimes \mathbb{I} - \eta\sigma_y \otimes \tau_z - \gamma\mathbb{I} \otimes \tau_y. \quad (16)$$

Here $\gamma \sim \alpha 8K^3$ [with $K = 4\pi/(3L)$] is due to the Rashba spin-orbit term (15) and is an energy scale that is comparable to the Rashba splitting Δ_R shown in Fig. 3(b). Again, this Hamiltonian is valid for $\mathbf{k} \sim 0$, and is an expansion about the $\mathbf{K}$ points; taking $v \to -v$ and $\gamma \to -\gamma$ one obtains the corresponding expansion about the $\mathbf{K'}$ points. We easily obtain the four eigenvalues of the effective Hamiltonian (16),

$$\mathcal{E}_k = \pm\sqrt{(v\mathbf{k} \pm \gamma)^2 + \eta^2}. \quad (17)$$

Hence the (gapped) Dirac cones are shifted from the $\mathbf{K}$ points ($\mathbf{k} = 0$) to $v\mathbf{k} \pm \gamma = 0$. It is easy to deduce the corresponding eigenvalues at the $\mathbf{K'}$ point, just by demanding the $\mathcal{T}$-symmetry condition: $\mathcal{E}_k^\uparrow = \mathcal{E}_{-k}^\downarrow$.

Overall, qualitatively, we find that the two degenerate copies of the band spectrum under $\mathcal{P}$ symmetry are now nondegenerate, and are simply momentum-shifted copies of each other. Most importantly, the topologically protected edge modes remain intact. Of course, taking into account momentum dependence of the Rashba term (15), see also Fig. 3(b), through the entire BZ will quantitatively change this conclusion from being a uniform momentum space shift to a momentum-dependent shift. But the salient point remains that breaking $\mathcal{P}$ symmetry does not destroy the TI state constructed here. We therefore need not worry about experimental inhomogeneities, or the influence of nonrectangular quantum well confinement geometries.

Additionally, one finds from the above calculation (or from [50] in the absence of Rashba) that the edge modes of the 1DP do not cross at the Γ point (unlike in the Kane-Mele model of graphene [6]). They are still $\mathcal{T}$-reversal-symmetric partners; they just do not cross in momentum space. Without further calculation we suggest that this offers two advantages over usual graphene: First, backscattering from a $\mathcal{T}$-breaking impurity (i.e., magnetic impurity) must satisfy a strict momentum conservation condition and hence it is conceivable that such backscattering events have a restricted phase space; i.e., the topological edge modes are equipped with an extra *protection*. Second, in a finite geometry the overlap of the wave functions of edge modes which occupy opposite edges of the sample is expected to produce a finite gap in the edge mode dispersions due to level repulsion. By the same argument as for the case of backscattering, the noncrossing of the edge mode dispersions in momentum space reduces the possibility of the finite geometry-induced level repulsion. We do not pursue these directions any further.

IV. CONCLUSIONS

We consider the topological insulating states of *artificial graphene*—generated by imposing a superlattice structure on top of a two-dimensional hole gas in a semiconductor heterostructure—and develop a method to calculate the band

structure. The method developed and presented here provides a nonperturbative treatment of the spin-orbit interaction and, in particular, is not limited to low energy/momentum scales. Previous approaches had precisely this limitation [50,51].

Using the developed technique we discuss the previously found *first set of Dirac points* (1DP), and confirm that they indeed represent a topological insulating state. Moreover, we point out an extra *protection* of the edge modes against magnetic impurities and finite geometry effects. We also perform a semianalytic, perturbative calculation to elucidate the effect of explicit parity (inversion) symmetry breaking, taking the particular case of a triangular well confinement. The analysis shows that parity breaking does not destroy the key properties of the topological edge states.

Our most important findings relate to what we call the *second set of Dirac points/bands*; these Dirac points sit at twice larger energy/momentum scales than the first set, and so have been completely beyond the validity of previous approaches to hole gas artificial graphene [50,51], although they were originally identified in electron gas artificial graphene [53], where spin-orbit interaction, and hence topological properties, was neglected. Our developed technique is indeed appropriate to describe the second Dirac bands, and we find the following desirable properties: (i) Owing to sitting at higher energy/momentum, the second Dirac bands experience larger spin-orbit interaction than the corresponding first Dirac bands, and hence possess a larger topological/spin-orbit band gap. With the present experimental limitations on the length scales d and L, this makes the topological insulating state obtained by tuning the Fermi energy to the second Dirac bands more robust than the topological insulating state obtained by tuning the Fermi energy to the first. (ii) The second Dirac bands possess three pairs of counterpropagating edge modes; the Chern number per spin species is $C_{\uparrow,\downarrow} = \pm 3$. Compare with the first Dirac bands, which have just a single pair of counterpropagating edge modes ($C_{\uparrow,\downarrow} = \mp 1$). (iii) Upon tuning the system parameters, we demonstrate the appearance of nearly flat bands endowed with a nontrivial topology ($C_{\uparrow,\downarrow} = \pm 3$). This finding suggests that hole-hole interactions become the dominant energy scale and as a result the system is expected to exhibit strongly correlated phases—most notably, a fractionalized topological insulator state, superconductivity, or exotic forms of magnetism.

In conclusion, the present work has exploited the highly tuneable nature of artificial graphene to show that it is an excellent candidate to realize (i) a topological band insulator phase, and (ii) a plethora of enigmatic, strongly correlated phases.

[1] M. König, S. Wiedmann, C. Brüne, A. Roth, H. Buhmann, L. W. Molenkamp, X.-L. Qi, and S.-C. Zhang, Science **318**, 766 (2007).

[2] I. Knez, R.-R. Du, and G. Sullivan, Phys. Rev. Lett. **107**, 136603 (2011).

[3] B. A. Bernevig, T. L. Hughes, and S.-C. Zhang, Science **314**, 1757 (2006).

[4] B. A. Bernevig and S.-C. Zhang, Phys. Rev. Lett. **96**, 106802 (2006).

[5] X.-L. Qi, Y.-S. Wu, and S.-C. Zhang, Phys. Rev. B **74**, 085308 (2006).

[6] C. L. Kane and E. J. Mele, Phys. Rev. Lett. **95**, 226801 (2005).

[7] E. Tang, J.-W. Mei, and X.-G. Wen, Phys. Rev. Lett. **106**, 236802 (2011).

[8] T. Neupert, L. Santos, C. Chamon, and C. Mudry, Phys. Rev. Lett. **106**, 236804 (2011).

[9] X. Hu, M. Kargarian, and G. A. Fiete, Phys. Rev. B **84**, 155116 (2011).

[10] N. Regnault and B. A. Bernevig, Phys. Rev. X **1**, 021014 (2011).

[11] S. Kourtis, J. W. F. Venderbos, and M. Daghofer, Phys. Rev. B **86**, 235118 (2012).

[12] Y.-L. Wu, B. A. Bernevig, and N. Regnault, Phys. Rev. B **85**, 075116 (2012).

[13] Y.-F. Wang, Z.-C. Gu, C.-D. Gong, and D. N. Sheng, Phys. Rev. Lett. **107**, 146803 (2011).

[14] J. W. F. Venderbos, S. Kourtis, J. van den Brink, and M. Daghofer, Phys. Rev. Lett. **108**, 126405 (2012).

[15] M. Levin and A. Stern, Phys. Rev. Lett. **103**, 196803 (2009).

[16] T. Neupert, L. Santos, S. Ryu, C. Chamon, and C. Mudry, Phys. Rev. B **84**, 165107 (2011).

[17] K. Sun, Z. Gu, H. Katsura, and S. Das Sarma, Phys. Rev. Lett. **106**, 236803 (2011).

[18] D. N. Sheng, Z.-C. Gu, K. Sun, and L. Sheng, Nat. Commun. **2**, 389 (2011).

[19] Y. Zhong, Y.-F. Wang, and H.-G. Luo, Phys. Rev. B **88**, 045109 (2013).

[20] M. O. Goerbig, Eur. Phys. J. B **85**, 15 (2012).

[21] S. A. Parameswaran, R. Roy, and S. L. Sondhi, C. R. Phys. **14**, 816 (2013).

[22] H. Katsura, I. Maruyama, A. Tanaka, and H. Tasaki, Europhys. Lett. **91**, 57007 (2010).

[23] T. Neupert, L. Santos, S. Ryu, C. Chamon, and C. Mudry, Phys. Rev. Lett. **108**, 046806 (2012).

[24] M. Hohenadler and F. F. Assaad, J. Phys.: Condens. Matter **25**, 143201 (2013).

[25] A. Kumar, R. Roy, and S. L. Sondhi, Phys. Rev. B **90**, 245106 (2014).

[26] R. L. Doretto and M. O. Goerbig, Phys. Rev. B **92**, 245124 (2015).

[27] S. Peotta and P. Törmä, Nat. Commun. **6**, 8944 (2015).

[28] V. J. Kauppila, F. Aikebaier, and T. T. Heikkilä, Phys. Rev. B **93**, 214505 (2016).

[29] M. Tovmasyan, S. Peotta, P. Törmä, and S. D. Huber, Phys. Rev. B **94**, 245149 (2016).

[30] M. Iskin, Phys. Rev. A **96**, 043628 (2017).

[31] L. Liang, T. I. Vanhala, S. Peotta, T. Siro, A. Harju, and P. Törmä, Phys. Rev. B **95**, 024515 (2017).

[32] B. Wunsch, F. Guinea, and F. Sols, New J. Phys. **10**, 103027 (2008).

[33] P. Soltan-Panahi, J. Struck, P. Hauke, A. Bick, W. Plenkers, G. Meineke, C. Becker, P. Windpassinger, M. Lewenstein, and K. Sengstock, Nat. Phys. **7**, 434 (2011).

[34] L. Tarruell, D. Greif, T. Uehlinger, G. Jotzu, and T. Esslinger, Nature (London) **483**, 302 (2012).

[35] T. Uehlinger, G. Jotzu, M. Messer, D. Greif, W. Hofstetter, U. Bissbort, and T. Esslinger, Phys. Rev. Lett. **111**, 185307 (2013).

[36] A. Singha, M. Gibertini, B. Karmakar, S. Yuan, M. Polini, G. Vignale, M. I. Katsnelson, A. Pinczuk, L. N. Pfeiffer, K. W. West *et al.*, Science **332**, 1176 (2011).

[37] C.-H. Park and S. G. Louie, Nano Lett. **9**, 1793 (2009).

[38] M. Gibertini, A. Singha, V. Pellegrini, M. Polini, G. Vignale, A. Pinczuk, L. N. Pfeiffer, and K. W. West, Phys. Rev. B **79**, 241406 (2009).

[39] L. Nádvorník, M. Orlita, N. A. Goncharuk, L. Smrčka, V. Novák, V. Jurka, K. Hruška, Z. Výborný, Z. R. Wasilewski, M. Potemski *et al.*, New J. Phys. **14**, 053002 (2012).

[40] S. Goswami, M. A. Aamir, C. Siegert, M. Pepper, I. Farrer, D. A. Ritchie, and A. Ghosh, Phys. Rev. B **85**, 075427 (2012).

[41] G. D. Simoni, A. Singha, M. Gibertini, B. Karmakar, M. Polini, V. Piazza, L. N. Pfeiffer, K. W. West, F. Beltram, and V. Pellegrini, Appl. Phys. Lett. **97**, 132113 (2010).

[42] F. D. M. Haldane and S. Raghu, Phys. Rev. Lett. **100**, 013904 (2008).

[43] S. Bittner, B. Dietz, M. Miski-Oglu, and A. Richter, Phys. Rev. B **85**, 064301 (2012).

[44] M. C. Rechtsman, J. M. Zeuner, Y. Plotnik, Y. Lumer, D. Podolsky, F. Dreisow, S. Nolte, M. Segev, and A. Szameit, Nature (London) **496**, 196 (2013).

[45] K. K. Gomes, W. Mar, W. Ko, F. Guinea, and H. C. Manoharan, Nature (London) **483**, 306 (2012).

[46] P. Ghaemi, S. Gopalakrishnan, and T. L. Hughes, Phys. Rev. B **86**, 201406 (2012).

[47] P. Kim and C.-H. Park, Nano Res. **9**, 1101 (2016).

[48] S. Klembt, T. H. Harder, O. A. Egorov, K. Winkler, R. Ge, M. A. Bandres, M. Emmerling, L. Worschech, T. C. H. Liew, M. Segev *et al.*, Nature (London) **562**, 552 (2018).

[49] M. Polini, F. Guinea, M. Lewenstein, H. C. Manoharan, and V. Pellegrini, Nat. Nanotechnol. **8**, 625 (2013).

[50] O. P. Sushkov and A. H. Castro Neto, Phys. Rev. Lett. **110**, 186601 (2013).

[51] T. Li and O. P. Sushkov, Phys. Rev. B **94**, 155311 (2016).

[52] T. Li and O. P. Sushkov, Phys. Rev. B **96**, 085301 (2017).

[53] O. A. Tkachenko, V. A. Tkachenko, I. S. Terekhov, and O. P. Sushkov, 2D Mater. **2**, 014010 (2015).

[54] D. S. Miserev and O. P. Sushkov, Phys. Rev. B **95**, 085431 (2017).

[55] T. Li, L. A. Yeoh, A. Srinivasan, O. Klochan, D. A. Ritchie, M. Y. Simmons, O. P. Sushkov, and A. R. Hamilton, Phys. Rev. B **93**, 205424 (2016).

[56] To obtain the topological winding number of each band, we calculate the Chern number per Kramers spin species; i.e., one can define the Berry curvatures $\mathcal{F}_{x,y}^{b,\sigma_b}$, where b labels the miniband and $\sigma_b = \uparrow, \downarrow$ labels the two Kramers spins, directly from the Hamiltonian (14) (or from its wave functions). As per usual, the Chern number for a given band and spin (b, σ_b) is then the integral of the Berry curvature over the entire Brillouin zone $C_{b,\sigma_b} = \int \mathcal{F}_{x,y}^{b,\sigma_b} dk_x dk_y / (2\pi)$. However, since we evaluate using a discrete (k_x, k_y) momentum grid, it is convenient to employ the *lattice gauge theory* technique of Ref. [58] to evaluate the C_{b,σ_b}. Due to $\mathcal{T}$ symmetry of the Hamiltonian $\mathcal{H}$ (14), it follows that (i) $\mathcal{H}$ can be made block diagonal in the Kramers spin index σ_b, and (ii) for a given band b, the Chern number is opposite in sign for each spin species, $C_{b,\downarrow} = -C_{b,\uparrow}$. The Chern numbers for the lowest four bands ($b \in \{1, 4\}$) in Figs. 5(b) and 5(c) are $C_{b,\uparrow,\downarrow} = \mp 1, \pm 1, \pm 0, \pm 3$.

[57] S. Kourtis and M. Daghofer, Phys. Rev. Lett. **113**, 216404 (2014).

[58] T. Fukui, Y. Hatsugai, and H. Suzuki, J. Phys. Soc. Jpn. **74**, 1674 (2005).